Effect of Selective Laser Melting Fabrication Parameters and Heat Treatment on the Microstructure and Mechanical Properties of Maraging 300 Alloy

Yaser Vahidshad[1*], Karen Abrinia[2]

[1] *Space Transportation Research Institute, Iranian Space Research Center, Tehran, Iran

*y.vahidshad@isrc.ac.ir

[2] Department of Mechanical Engineering, College of Engineering, University of Tehran, Tehran, Iran

Abstract

Selective laser melting (SLM) is a widely used additive manufacturing method for 3D-printing metal parts. This study investigates how SLM parameters affect the density, microstructure, and mechanical properties of maraging steel 300. A process window was developed, revealing that maximum density and minimal porosity are achieved when laser energy density exceeds 50 J/mm³. Optimal parameters—100 mm/s scan speed, 20 μm layer thickness, 0.15 mm hatch distance, Stripe scanning strategy, and XZ build direction—were identified. Optimal processing reduced porosity, increased martensite content, and enhanced strength, reaching 1064 MPa and improving by 75% to 1862 MPa after aging and solution treatment. Strength gains were attributed to the uniform dispersion of nano-sized precipitates (such as $Ni(Mo)_3$ and $Ni(Ti, Al)_3$) within the martensitic matrix. Additionally, it was found that higher cooling rates further improve the mechanical strength of heat-treated parts.

Key words: Additive manufacturing, Selective laser melting, Maraging steel, Heat treatment, Microstructure.

1- Introduction

Typically, metal parts are produced using two methods: forming methods such as casting, shaping, welding, and reduction methods such as machining. In recent decades, powder metallurgy methods have also been used to produce complex and special parts. Although these methods are widely used, each has its own limitations, and different manufacturing methods are chosen for different parts based on these limitations [1]. The additive manufacturing (3D printing) method, which is somehow similar to the powder metallurgy method, has many advantages over the previous conventional methods. Materials such as metals, ceramics, plastics, and composites can be used in this process. Through computer integration and innovative ideas, additive manufacturing has created an impressive and extensive industrial transformation that many have referred to as one of the major axes of the fourth industrial revolution [2-5].

Additive manufacturing method of maraging steel alloys plays an important role in making complex parts and structures that are difficult or in some cases impossible to build using traditional methods. In general, the additive manufacturing method has many advantages such as cost savings, weight reduction, production based on demand, reduction of manufacturing time and integration for parts used in automotive [6], biomedical (implants, prostheses) [7-9], aerospace (aerospace structures, tank, combustion chamber and nozzle) [10-12], power plant (turbine blade) [13-15], petrochemical (ceramic catalyst base) [16] and instruments [17]. Maraging steels have excellent mechanical properties (high strength at ambient temperature and high temperature, and good toughness), are heat treatable, and have good machining and forming properties. There are two main alloy groups of maraging steel: those with cobalt and those without cobalt. They are more expensive than other steel alloys due to the presence of many alloy elements (Ni, Co, W, Mo). The high strength is attributed to the strengthening of precipitates compounds (such as Fe_2Mo, $NiAl$, $Ni_3(Ti, Al, Mo)$, $Ni(Al, Fe)$) with homogeneous distribution in the matrix after thermal aging. The high toughness and ductility are due to the relatively soft martensitic background in the absence of carbon, which makes it optimally malleable. Maraging alloys have very good welding properties due to their low interstitial elements (such as carbon) [18-21].

Over the last few years, a lot of research has been done on how additive manufacturing and heat treatment affect maraging steel's metallurgical and mechanical properties [12, 18]. These parameters include laser power,

1 scanning speed, hatch distance, strategy, layer thickness, manufacturing direction, laser source, and type of

2 powder (morphology, size, production method) [22, 23].

3 **Table 1 Research conducted on the parameters of additive manufacturing of Maraging 300 steel**

Researcher	Laser power Watt		Scan speed mm/sec.		Hatch Distance mm		Layer thickness mm		Strategy	Building direction		Powders size µm	Ultimate strength MPa
Bai et al. [24]	100 130	160 190	300 400	500 600	0.05 0.07	0.09 0.11	0.04		-	-		15-45	1177* 2163#
Becker et al. [25]	200		600 800	1000	0.075 0.105	0.135	0.03		Single Double	Y Z		43	1205* 1850#
Casalino et al. [26]	57 86	100	180 200	220	0.14		0.03		Randomly selected sector	-		40	1100* -
de Souza et al. [27]	400		600 900	1200 1500	0.1		0.045 0.055	0.065 0.075	-	X Z 45		16.7	1232* -
Shamsdini et al. [28]	285 305		960 1010		0.11		0.04 0.05		Stripe	X		40	1225* -
Huang et al. [29]	180 220	260 300	500 700	900 1100	0.08 0.11	0.14 0.17	0.020 0.035	0.050 0.065	-	-		30	- -
Mugwagwa et al. [30]	80 100 120 140 160 180		200 300 400 500 600 700 800 900 1000		0.105		0.030 0.045		Island Stripe	-		-	- -
Suzuki et al. [31]	40 60 80 100 120 140 160 180 200 220 240 260		500 1000 1500 2500		0.050		0.030		-	-		-	- - -
Mutua et al. [32]	100 150 200 250 300 350 400		400 500 600 700 800 900 1000		0.025 0.050 0.075 0.1 0.125 0.150 0.200		0.020		-	X		20	1125* 2033#
Hu et al. [33]	300		920		0.110		0.050		-	-		1553	1002* 1883#
Vishwakarma et al. [34]	400		200		0.080		0.040		-	-		-	1073* 1568 #
Yao et al. [35]	380		960		0.110		0.040		Stripes	X Z		15-62	1123* 1877#
Patil et al. [36]	180 285 390		800 1000 1200		0.08 0.10 0.12		0.02 0.04 0.06		Stripe	-		10-48	1322* -
[37]	200-370		500-2300		0.050-0.150		0.040		zigzag	X		42	1165* 1943#
Monkova et al. [38]	280		960		0.110		0.040		Stripe	-		-	1200* 2050#
Kannan et al. [39]	100 145 190		1000 1500 2000		0.050 0.080 0.110		0.045		-	X		-	- -

* As built   , # Solution treatment and aging

4

1   Table 1 summarizes the research findings on how key parameters affect the metallurgical and

2   mechanical properties of maraging 300 steel parts. The results emphasize the need for a minimum

3   laser energy density to achieve optimal part density, while excessive energy can cause gas porosity

4   from metal vaporization. Among the energy density factors, laser power and layer thickness have the

5   greatest impact on reducing porosity and increasing density, whereas scan speed and hatch distance

6   play a lesser role. The scanning strategy also significantly influences porosity and residual stress

7   reduction. However, as a result of many cracks and pores inside the parts, the strength of maraging steels

8   produced by SLM cannot exceed 2000 MPa [24-39].

9   Understanding how process parameters affect relative density is vital in additive manufacturing,

10   which produces unique microstructures even after heat treatment. Optimization is challenging due to

11   variations in parameters, machines, and powders. This study examines the effects of scanning speed,

12   hatch distance, and build direction on the microstructure and mechanical properties of maraging 300

13   steel. A process map was developed to optimize parameters and improve part quality. The effects of

14   solution treatment, aging, and, for the first time, cooling rate on the mechanical properties of

15   optimized samples were also investigated.

16   **2- Experimental procedure**

17   Samples were produced using an EOSINT M250 machine (EOS), featuring a 200 W laser, 300 μm

18   beam diameter, and 1060 nm wavelength. Figure 1 shows the schematic of the SLM process

19   parameters under study. Based on Table 1, scanning speed, melt pool center-to-center distance, and

20   beam direction were analyzed, while laser power and particle size remained constant. To limit sample

21   production, a single scanning strategy was chosen. MS1 steel powder (EOS, Germany) was used for

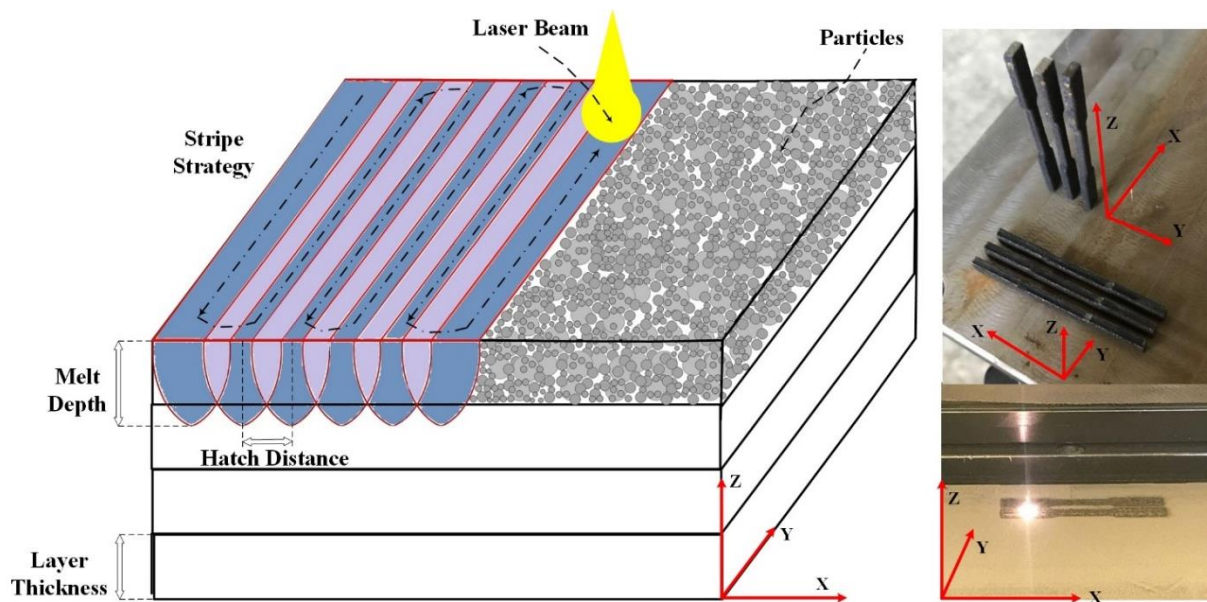22   fabricating maraging 300 steel parts.

4

Figure 1 Schematic of the selective laser melting process (left) and fabricated maraging 300 samples (right).

Table 2 presents the chemical composition and physical properties of maraging 300 steel. Test samples, shaped as flat tensile specimens (Figure 2(a)), were designed in CAD software, saved in STEP format, and prepared for printing with Materialise Slicer. After fabrication under argon, samples were separated from the substrate via wire cutting. Tensile testing was performed using an AUTOGRAPH AG-25TC machine (25 kN capacity) at a crosshead speed of 1 mm/min. Due to surface roughness from printing, all samples were polished post-production. Hardness was evaluated using Avery-Denison's AG-25TC device. Porosity, microstructure, and phases were analyzed using a Leica DM 4000 M optical microscope (OM) and a MIRA3 TESCAN FESEM.

Table 2 Chemical composition and morphology of maraging grade 300 steel powder (MS1)

Element	Fe	Co	Ni	Mo	Ti	Al	Cu	Cr	Si	Mn	C
%	Balance	8.5-9.5	17-19	4.5-5.2	0.6-0.8	0.05-0.15	0.5	0.5	0.1	0.1	0.03
Mean particle size				**Maximum particle size**				**Particle density**			
40 μm				63 μm				8-8.1 g/cm^3			

5

1 **3- Results and Discussion**

2 **3-1- Initial optimization of manufacturing parameters by Taguchi method**

3   Porosity in selective laser melting (SLM) stems from mechanisms such as lack of fusion, keyhole

4 formation, gas entrapment, powder defects, improper layer thickness, and process instabilities which

5 understanding these is essential for enhancing part quality [40-41]. A previous study [42] showed that

6 porosity increased sharply as scanning speed rose from 70 to 130 mm/s, due to reduced energy density

7 (Inadequate energy input) causing incomplete melting of powder particles. Similarly, increasing layer

8 thickness from 20 to 60 μm raised porosity, primarily because powder particles, averaging 50

9 microns, with some exceeding 60 (Irregular powder morphology), did not fully melt at greater

10 thicknesses, further worsened by declining energy density. Porosity increased notably as hatch

11 spacing widened from 0.2 to 0.3 mm, due to reduced overlap and Inadequate energy input (incorrect

12 hatch spacing) causing incomplete melting. Additionally, the stripe scan strategy showed lower

13 porosity than the chessboard pattern, likely due to more stable melt pools (scanning path errors) and

14 improved microstructural uniformity.

15   In our previous study [42], a Taguchi model was used to investigate scanning speed, layer thickness, hatch

16 distance, and scanning strategy. Samples produced with a scan speed of 70 mm/s, 0.2 mm layer thickness,

17 0.2 mm hatch distance, and a straight-line stripe scanning strategy showed the lowest porosity and highest

18 strength. Each parameter set was tested on three samples, and results were averaged. Higher energy densities

19 (>60 J/mm³) reduced porosity to below 0.5% (Figure 2(b)) and enhanced strength by minimizing

20 stress concentrations. Red areas in Figure 2(b) indicate unmelted powder or pores. These results

21 prompted further investigation into hatch distance, scanning speed, build direction, and heat

22 treatment.

6

Figure 2 a) dimension of fabricated tensile specimen, b) the effect of energy density on the porosity of parts made by SLM.

3-2- Hatch distance

Based on to the hatch distance parameter, the ultimate tensile strength value increased at hatch distances of 0.1 mm and 0.15 mm due to an increase in energy density and a decrease in porosity. According to the results, the overlapping distance parameter had a greater effect than the laser scanning speed parameter. Thus, the hatch distance of 0.15 mm had a relatively higher strength than 0.1 mm. Among the samples produced with a 0.15 mm hatch distance, the strength of samples S22 and S23 was nearly equal and higher than that of the other samples. More detailed investigation indicated that a 70 mm/s scanned sample (S22) had surface burn compared to a 100 mm/s scanned sample (S23). Therefore, to choose the optimal surface roughness, whose mechanical properties, repeatability, standard deviation, and porosity were very close to each other, based on the physical appearance of the samples produced on these two surfaces, S23 was the best. A comparison of the mechanical and physical properties of the samples (optimal sample conditions) indicated that if the minimum energy density number was around 50-60 J/mm^3, the minimum porosity (less than 1%) was obtained as well as optimal mechanical properties (Table 3). When the energy density was lower than 40 J/mm^3, large pores and unmelted particles appeared inside the part. When the energy density exceeded 70 J/mm^3, the porosity did

7

1 not decrease any further. Porosity was sometimes caused by the evaporation of the molten pool at high energy

2 density. Due to this, the mechanical properties of the parts were reduced.

3 **3-3- Build direction**

4 The construction direction was studied after obtaining the optimal hatch distance and scanning speed.

5 Therefore, using 0.15 mm hatch distance, 100 mm/s scanning speed, 0.20 layer thickness, and stripe scanning

6 strategy, samples were made in three directions X-Y, X-Z, and Z-Y. There was almost no difference in the

7 ultimate tensile strength of the samples made in the XY and XZ directions, although the XZ direction exhibited

8 a slightly higher strength value than the XY direction. Three samples were compared based on their ultimate

9 tensile strength results, and the part fabricated in the X-Z direction had higher strength than the other two

10 (Table 3). Due to the lower contact surface of the powder melting zone with the metal substrate, the heat

11 transfer rate was lower in the ZX direction than it was in the other two directions. Because of this, less

12 martensite phase was formed (more austenite remains), thus reducing strength. Therefore, after checking the

13 above parameters, the optimal conditions are made in the form of 0.15 mm hatch distance, 100 mm/s scanning

14 speed, 0.02 mm layer thickness, stripe scanning strategy and X-Z direction.

15

16 **Table 3 Examining results of hatch distance, scanning speed, layer thickness, strategy scan and build**

17 **direction parameters.**

Sample	Build Direction	Strategy Scan	Layer Thickness mm	Scanning Speed mm/s	Hatch Distance mm	Energy Density J/mm³	Porosity %	Ultimate Strength MPa	Hardness HB	
									Transverse	Longitudinal
S19				70	0.1	142. 9	0.6	948	322	351
S20				100	0.1	100.0	1.9	938	350	369
S21				130	0.1	76.9	1.7	938	363	378
S22				70	0.15	95.2	0.05	950	350	363
S23	X-Y			100	0.15	66. 7	0.6	951	349	353
S24		Stripe	0.02	130	0.15	51.3	0.6	946	345	354
S1				70	0.2	71.4	0.5	885	371	349
S25				100	0.2	50.0	4.5	798	347	356
S4				130	0.2	38.5	6.5	729	305	297
S23	X-Y					66. 7	0.6	950	349	353
S26	X-Z			100	0.15	66. 7	0.4	964	299	283
S27	Z-X					66. 7	0.4	921	351	307

18

Figure 3 shows the optical microscope image of the cross-section of the printed tensile sample in X-Y, X-Z and Z-X directions. On the 200x optical microscope image of S23 and S26 samples (Figure 3(a), (d)), parallel layers formed by laser melting scanning could be observed. The line illustrates the effect of turning on and off the laser beam that is perpendicular to the layers (bead like). Layer traces and laser effect lines have a size of 25 to 35 μm. Based on the higher magnification images (500x and 1500x), it could be seen that the thermal gradient was perpendicular to the layers. It is due to the fact that the thermal flux was directed towards the metal substrate under the powder (Figure 3(b), (e), (c), (f)). Since the ratio of G/R decreased from the melting borders to the center of each bead, a columnar structure generally appeared from the sides of the melting borders to the coaxial structure inside. Therefore, the observed microstructure consists of columnar structure (perpendicular to the bottom metal base plate) along with cellular structure. As a result of low heat input and rapid cooling, martensite forms in additive manufacturing methods. In parts S23 and S26, martensite lath (light color) dominates the microstructure probably with a small amount of retained and reverted austenite (Figure 3(c), (f)). Sample S26 differs from sample S23 only in the direction of the print layers affected by the scan lines of the molten pool, which could be observed with a 90° angle (Figure 3(a), (d)). Both cellular and columnar microstructures could be seen on both sides of the melting line. Based on the comparison of samples S23 and S26 (Figure 3(c), (f)), it is evident that sample S23 contains significantly more martensite phase and columnar solidification structure than sample S26, which is due to the greater contact surface in the XY direction of the sample with the metal substrate, which transfers more heat and causes the part to cool faster. The results of the X-ray diffraction (XRD) test indicate that the primary phase formed in Sample No. 26 (the optimized sample without heat treatment) consists of martensite and, to some extent, austenite (Figure 4).

The optical microscope image of the printed tensile sample in the Z-X direction (200x) does not show any layer effects (layer tracks) because the optical microscope shows the surface of the layer (Figure 3(g)). It is evident from the image with higher magnification (500 and 1500 times, Figure 3(h), (i)) of sample S27 that due to the area of the lower surface of the sample in the Z-X direction at the point of contact with the metal substrate under the samples, the heat transfer rate is reduced, and directional solidification has been replaced with more coaxial solidification (cellular solidification structure).
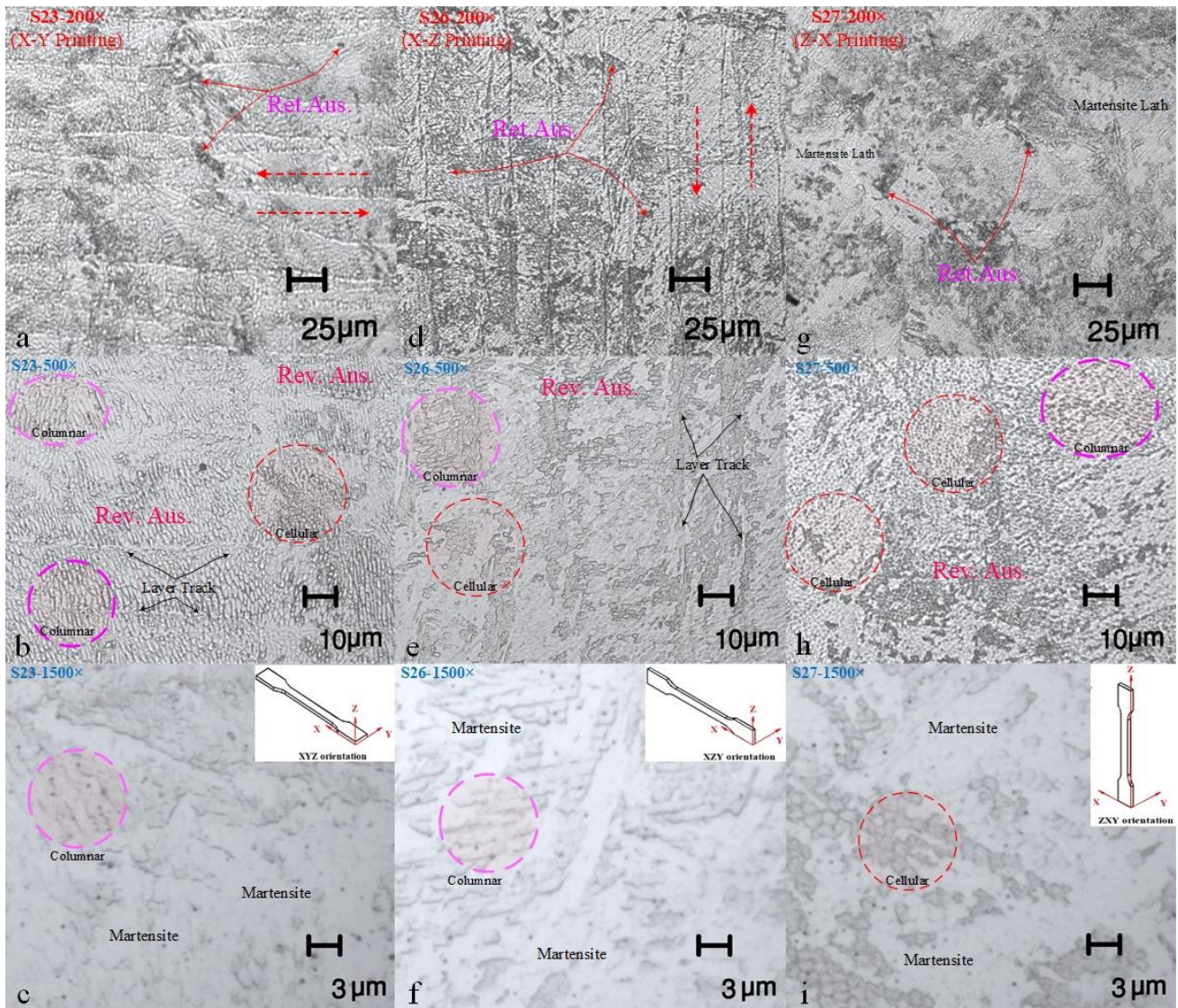
Figure 3 Microstructure of parts produced in three directions XY (S23), XZ (S26) and ZX (S27).

10

Figure 4 The XRD results of the sample of S26.

3-4- Heat treatment effect

The effects of heat treatment on SLM maraging steel on its microstructural and mechanical properties changes are investigated and discussed in this section. Based on the design of the experiments conducted in this section, the experiments were conducted in three parts, with the final goal of obtaining the optimal mechanical properties for the solution and aging heat treatment. After solution treatment at 820°C for an hour, each sample was aged at 420°C, 480°C, and 540°C for 5 hours, in order to investigate the effect of aging temperature. Figure 5 shows the microstructure of heat-treated samples at different aging temperatures. Unlike the images in Figure 3, where the samples have not been heat treated and the melting boundary of the layers is

11

1 clearly visible (sample S26), the melting boundary of the layers is not observed in the heat-treated samples

2 (samples of S30, S31 and S32).

3   At the appropriate solution temperature and time, these melting boundaries (layer track) dissolve and

4 disappear. The conducted research showed that due to the low solubility of Mo and Ti in the solid phase

5 compared to the liquid phase and rapid solidification of the melt in the additive manufacturing method, these

6 two elements remain at the grain boundary and Mo and Ti rich areas were formed. Furthermore, the broken

7 bonds in the grain boundaries created more space for soluble elements in the grain boundaries. These

8 boundaries include solidification grain boundaries, martensite plate boundaries, and austenite-martensite

9 boundaries. When the solution treatment was occurred, it caused molybdenum and titanium to find enough

10 energy to penetrate into the grains, so the melting track and grain boundaries began to break and dissolve [43-

11 46].

Figure 5 The microstructure of the samples produced in the optimal state in the XZ direction for three solution treatment samples at a temperature of 820ºC, cooled in water and aged at a temperature of 540ºC (S30), 480ºC (S31) and 420ºC (S32).

13

1   On the other hand, the dissolution of Mo and Ti in solution heat treatment stage causes the formation of a

2   supersaturated solid solution in the matrix after fast cooling of the sample (water quenching) and the formation

3   of martensite. The aging treatment causes the formation of intermetallic precipitations consisting of Mo and

4   Ti with appropriate distribution and size in the matrix. The formation of these precipitations increases the

5   strength of maraging steel alloy by almost twice the initial value, after heat treatment (Table 4).

6   This is one of the reasons that the samples fabricated by additive manufacturing are better not to be directly

7   aged. Hence before aging, they undergo a solution heat treatment in order to dissolve the alloy elements such

8   as Mo and Ti to make them uniform in the matrix phase. Figure 6 shows the EDS analysis at the points marked

9   with capital letters. In sample S31 (Figure 6(d), (e)), the best barrier for the movement of dislocations is

10   obtained due to the precipitation of particles with the optimal size and population. The highest ultimate tensile

11   strength with 1670 MPa was obtained at 480°C (S31). According to the Orowan mechanism, coarsening of

12   particles leads to a decrease in precipitation population (dissolving of smaller particles) and an increase in

13   precipitation distance, thereby reducing dislocation hindrance [47].

14   The sample S30 which was age hardened at temperature of 540°C lost its strength due to coarsening of

15   intermetallic precipitations such as $Ni_3(Mo)$ in the matrix (Figure 6(b)), resulted in an increase in the distance

16   between formation precipitations, so dislocations pass more easily between these precipitated particles. The

17   ultimate tensile strength of the sample was 1413 MPa (S30) which was lower than S31 sample. When age

18   hardening occurs at 420°C instead of 480°C, the thermal energy required to penetrate elements such as Mo and

19   Ti to continue the growth of precipitated particles is insufficient, and the particles are not able to reach the

20   ideal size as a result. Therefore, dislocations could easily shear and pass through precipitation due to their small

21   size and greater distance from each other (Figure 6(g)). Thus, this sample (S32) has a lower ultimate tensile

22   strength as compared with samples age hardened at temperatures 540°C (S30) and 480°C (S31).

23   According to the chemical composition percentage (Table 5), fine precipitations are mostly $Ni_3(Ti, Al, Mo)$

24   and Ni_3Mo (intermetallic compounds). In austenite or martensite phase, Fe and Ni is a major element of the

25   matrix chemical composition.

14

Table 4 The effect of heat treatment parameter on the mechanical properties of the optimal additive manufacturing sample.

Sample	Heat Treatment	Parameters	Fabrication Direction	Scan Strategy	Layer Thickness mm	Scan Speed mm/s	Hatch Distance mm	Porosity %	Ultimate Strength MPa	Hardness (HB) Transverse	Longitudinal
S26	Without heat treatment	Without heat treatment						0.4	964	299	283
S30	S.T. 820ºC, W.Q., Aging 540ºC							0.4	1413	445	465
S31	S.T. 820ºC, W.Q., Aging 480ºC	Effect of aging temperature						0.4	1670	505	521
S32	S.T. 820ºC, W.Q., Aging 420ºC		X-Z	Stripe	0.02	100	0.15	0.4	1182	451	445
S31	S.T. 820ºC, W.Q., Aging 480ºC							0.4	1670	505	521
S33	S.T. 820ºC, A.C., Aging 480ºC	Effect of cooling rate on solution treatment temperature						0.4	1300	455	461
S34	S.T. 820ºC, F.C., Aging 480ºC							0.4	1265	448	455

S.T. : Solution Heat Treatment , W.Q. : Water Quenching

Fine precipitations are mainly scattered in the matrix, Mo is more visible at grain boundaries, hence even after heat treatment, some Mo remains at the grain boundary and forms precipitations of Ni_3Mo (Figure 6(e)). It is observed that the particle size of the aged hardening sample (S31) at 480°C is mainly less than 20 nm, while the particle size of the aged hardening sample (S30) at 540°C is mainly larger than 50 nm. A comparison of the nickel content in the matrix phase of the sample hardened at 540°C with that of the other two samples shows that the sample age hardened at 540°C (Figure 6(a)) has a more reverted austenite phase (Figure 6(c), (f)) which can be seen as white piecemeal regions. Additionally, precipitation particles change from spherical to worm- or rod-shaped (S30) as aging temperature increases (Figure 6(b)). Figure 7 shows EDXS maps of the heat-treated sample (S31). According to the EDXS map of the hardened sample at 480°C, Mo, Ni, Co, and Fe elements are evenly distributed. The presence of more Mo, Ti, and Al elements in certain areas indicates that the $Ni_3(Mo, Ti, Al)$ intermetallic particles have been precipitated.
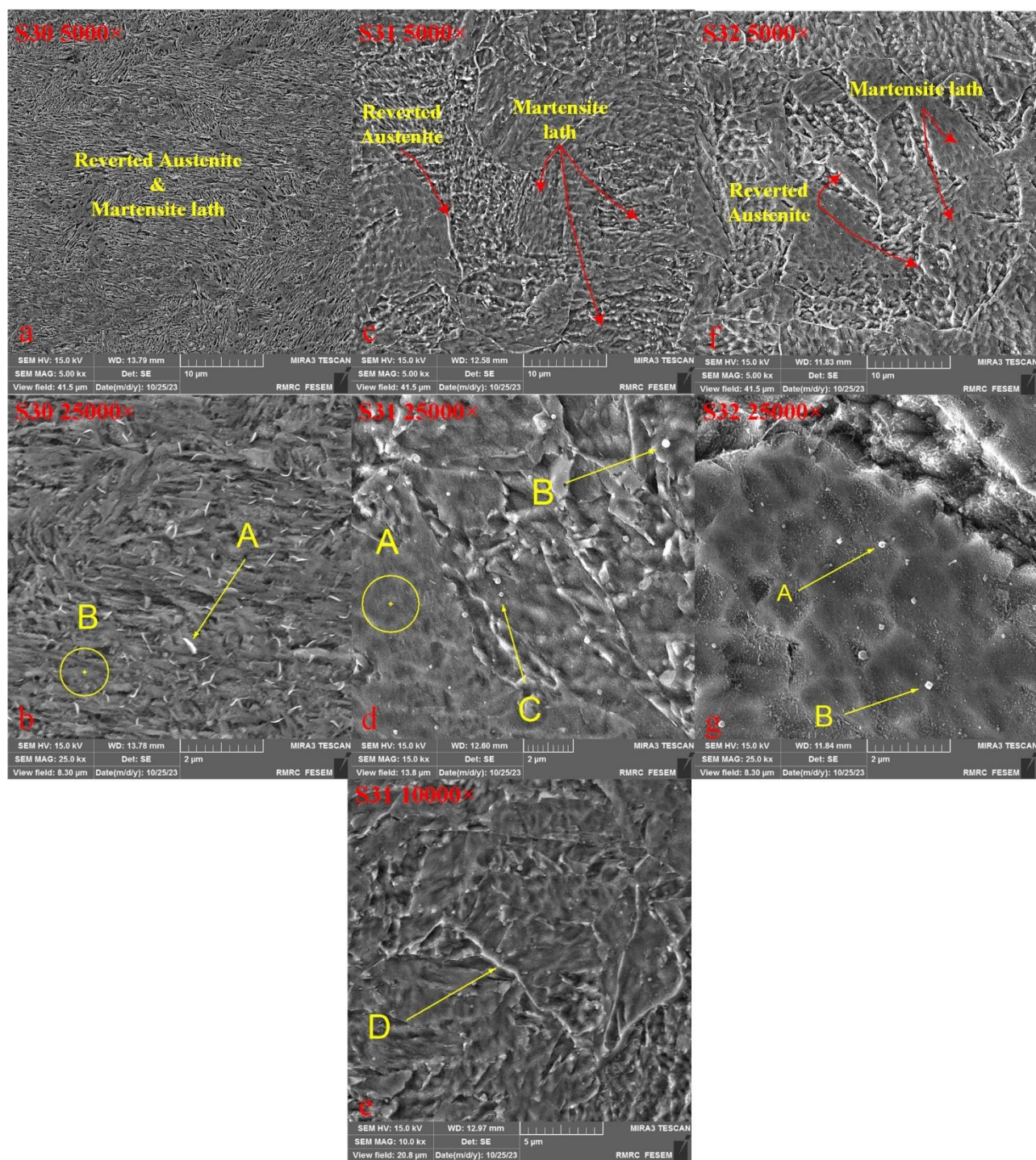
15

Figure 6 Scanning electron microscope images of the sample produced in the optimal state in the XZ direction for three solution treatment samples at a temperature of 820ºC, cooled in water and aged at a temperature of 540ºC (S30), 480ºC (S31) and 420ºC (S32).

16

Table 5 Chemical composition of (yellow arrowed) the employed powder determined by EDX analysis.

| Sample	Point	Atomic percent						Compound
		Ni	Ti	Al	Mo	Co	Fe	
S30 (Aged at 540°C)	A	17.45	0.47	0.51	7.90	7.12	66.54	Precipitation - $Ni_3(Mo)$
	B	19.55	0.71	0.55	7.59	7.41	64.19	Matrix
S31 (Aged at 480°C)	A	15.95	0.4	0.41	9.45	8.15	69.31	Matrix
	B	14.79	4.61	3.15	6.65	7.56	63.24	Precipitation - $Ni_3(Ti, Mo, Al)$
	C	16.19	1.46	0.98	5.69	8.10	67.58	Precipitation - $Ni_3(Ti, Mo, Al)$
	D	16.05	0.66	0.44	5.97	8.35	68.53	Boundary
S32 (Aged at 420°C)	A	16.19	2.14	1.19	6.27	7.89	63.32	Precipitation - $Ni_3(Mo, Ti, Al)$
	B	14.95	2.82	0.55	5.62	8.34	67.72	Precipitation - $Ni_3(Mo, Ti, Al)$
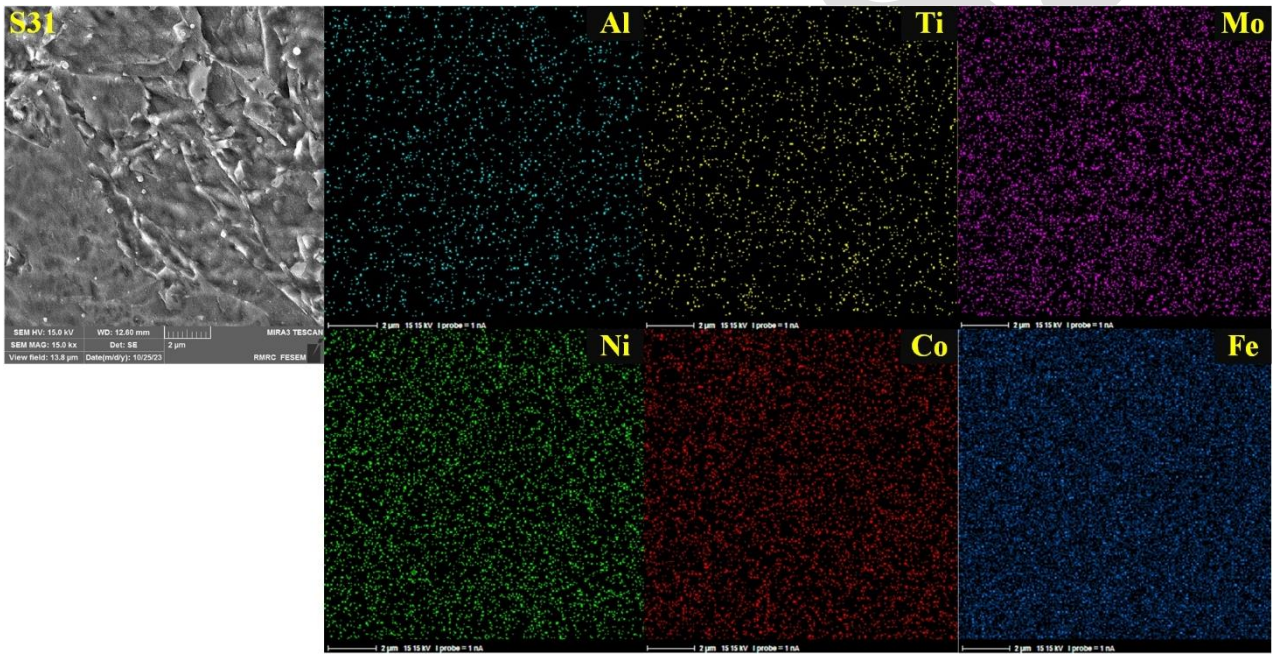
Figure 7 EDXS map of sample solution treated at 820ºC, cooled in water (S31) and aged at 480ºC.

A maraging steel alloy's strength is significantly affected by the cooling rate from the solution heat treatment stage. The matrix rich in Ni, Co, Ti, Mo, and Al can precipitate secondary phases when cooled with water at the maximum rate immediately after leaving the furnace due to a supersaturated solid solution (SSSS). As a result, the number of precipitated particles and their distribution will be the best. Additionally, due to the high cooling rate (Figure 8(a), (b)), the martensite phase also reaches its maximum value, resulting in the

17

strength of sample being at its highest value after aging, compared to samples cooled at a lower rate. In fact, a low cooling rate (air (Figure 8(c), (d)) or furnace cooling (Figure 8(e), (f))) causes less martensite to form during cooling, resulting in more austenite remaining (retained austenite). As the austenite content in the sample increased, the sample's strength decreased.

Figure 8 Scanning electron microscope micrographs of samples solution treated at 820ºC, cooled in water (S31), air (S33) and furnace (S34) and aged at 480ºC.

4- Conclusions

This paper investigates the selective laser melting (SLM) process parameters in relation to heat treatment, with a focus on precipitation morphology under various heat treatment conditions. A series

18

of SLM parameters, including hatch distance, scanning speed, layer thickness, scanning strategy, and build direction, were applied to maraging steel samples produced via SLM. The study explores the evolution mechanisms of microstructure, tensile properties and microhardness under different heat treatment regimes. The following conclusions can be drawn from this work:

1) To achieve a structure with minimal porosity and eliminate unmelted particles, the energy density must be at least 50 J/mm³. At this threshold, porosity remains below 1%.

2) Among the tested laser scanning speeds (70, 100, and 130 mm/s), the highest tensile strength is achieved at 100 mm/s. Porosity increases with higher scanning speeds. For hatch spacings of 0.1, 0.15, and 0.3 μm, the optimal strength is obtained at 0.15 μm, though porosity consistently increases with wider hatch spacings. As layer thickness increases from 0.2 to 0.6 μm, both ultimate tensile strength and overall part density decrease due to the rise in porosity.

3) Using a stripe scanning strategy results in a 35% increase in tensile strength, a 12% increase in hardness, and a 45% reduction in porosity compared to the chessboard strategy. The ultimate tensile strength varies with build orientation: 950 MPa in the XY direction, 964 MPa in the XZ direction, and 921 MPa in the ZX direction.

4) Heat treatment significantly enhances mechanical properties, increasing ultimate tensile strength by approximately 75%—from 964 MPa to 1670 MPa. The optimized sample after heat treatment exhibits a microstructure consisting of cellular and acicular martensite, along with some retained austenite. Intermetallic precipitates, such as $Ni(Mo)_3$ and $Ni(Ti, Al)_3$, are uniformly dispersed within the matrix, contributing to the increased strength.

5) The highest tensile strength is achieved by rapidly quenching the sample in water after solution treatment at 820 °C, followed by aging at 480 °C.

19

1 **Competing of interests**

2 The authors declare that they have no known competing financial interests or personal relationships that could

3 have appeared to influence the work reported in this paper.

4

5 **References:**

[1] Kumar, S., "Technology of metal forming processes", PHI Learning Pvt. Ltd, 2008.

[2] Prashar, G, Vasudev, H., Bhuddhi, D., "Additive manufacturing: expanding 3D printing horizon in industry 4.0", Int. J. Interact. Des. Manuf., 2023,17, 2221–2235. https://doi.org/10.1007/s12008-022-00956-4

[3] Bajaj, P., Hariharan, a., Kini, A., Kürnsteiner, P., Raabe, D., Jägle, E.A., "Steels in additive manufacturing: A review of their microstructure and properties", Mater. Sci. Eng., A, 2020, 772, 138633. https://doi.org/10.1016/j.msea.2019.138633

[4] Sun, J., Ye, D., Zou, J., Chen, X., Wang, Y., Yuan, J., Liang, H., Qu, H., Binner, J., Bai, J., "A review on additive manufacturing of ceramic matrix composites", J. Mater. Sci. Technol. 2023, 138, 1-16. https://doi.org/10.1016/j.jmst.2022.06.039

[5] Gardner, L. "Metal additive manufacturing in structural engineering – review, advances, opportunities and outlook", Structures 2023, 47, 2178-2193. https://doi.org/10.1016/j.istruc.2022.12.039

[6] Ahmadi, M., Bozorgnia Tabary, S.A.A., Rahmatabadi, D., Ebrahimi, M.S., Abrinia, K., Hashemi, R., "Review of selective laser melting of magnesium alloys: advantages, microstructure and mechanical characterizations, defects, challenges, and applications", J. Mater. Res. Technol. 2022, 19, 1537-1562. https://doi.org/10.1016/j.jmrt.2022.05.102

[7] Sankaranarayanan, S., Gupta, M., "Emergence of god's favorite metallic element: Magnesium based materials for engineering and biomedical applications", Part 1, Mater. Today Proc. 2021, 39, 311-316. https://doi.org/10.1016/j.matpr.2020.07.220

20

[8] Jamshidi, P., Aristizabal, M., Kong, W., Villapun, V., Cox, S. C., Grover, L. M., Attallah, M. M., "Selective laser melting of Ti-6Al-4V: the impact of post-processing on the tensile, fatigue and biological properties for medical implant applications", Materials, 2020, 13, 2813. https://doi.org/10.3390/ma13122813

[9] Zhang, H. W., Xu, Y. L., Chen, L. J., Wang, X. W., Wu, Z. Y., Li, S., Li, J., Xiao, X. S., "Precipitation behaviors of a new antibacterial maraging stainless steel for medical instruments", Metall. Mater. Trans. A, 2018, 49, 3753-3761. https://doi.org/10.1007/s11661-018-4733-x

[10] Kurzynowski, T., Pawlak, A., Smolina, I., "The potential of SLM technology for processing magnesium alloys in aerospace industry", Arch. Civ. Mech. Eng., 2020,20, 23. https://doi.org/10.1007/s43452-020-00033-1

[11] Mouritz, A. P., "Introduction to aerospace materials", Woodhead Publishing, 2012.

[12] Li, K., Yang, T., Gong, N., Wu, J., Wu, X., Zhang, D. Z., Murr, L. E., "Additive manufacturing of ultra-high strength steels: A review", J. Alloys Compd., 2023, 965, 171390. https://doi.org/10.1016/j.addma.2024.104496

[13] Sing, S. L., Yeong, W. Y., Wiria, F. E., Tay, B. Y., Zhao, Z., Zhao, L., Tian, Z., Yang, S., "Direct selective laser sintering and melting of ceramics: A review", Rapid Prototyping J., 2017, 23, 611-623. https://doi.org/10.1108/RPJ-11-2015-0178

[14] Sims, C. T., Stoloff, N. S., Hagel, W. C., "Superalloys II: Heat-resistant materials for aerospace and power plants", Wiley, 1987.

[15] Ealy, B., Calderon, L., Wang, W., Kapat, J., Mingareev, I., Richardson, M., Valentin, R., "Characterization of LAM-fabricated porous superalloys for turbine components", in proceedings of the ASME Turbo Expo 2016: Turbomachinery Technical Conference and Exposition, Seoul, 2016.

[16] Mozammel, T., Dumbre, D., Selvakannan, P. R., Sadasivuni, K. K., Bhargava, S. K., "Calcined hydrotalcites of varying Mg/Al ratios supported Rh catalysts: highly active mesoporous and stable

catalysts toward catalytic partial oxidation of methane", Emergent Mater., 2021, 4, 469-481. https://doi.org/10.1007/s42247-020-00158-2

[17] R. R. C., "The Superalloys: Fundamentals and Applications", Cambridge, 2006.

[18] Hadadzadeh, A., Shahriari, A., Shalchi Amirkhiz, B., Li, J., Mohammadi, M., "Additive manufacturing of an Fe–Cr–Ni–Al maraging stainless steel: Microstructure evolution, heat treatment, and strengthening mechanisms", Mater. Sci. Eng. A, 2020, 787, 139470. https://doi.org/10.1016/j.msea.2020.139470

[19] Sha, W., Guo, Z. "Maraging steels: modelling of microstructure, properties and applications", Woodhead Publishing, 2009.

[20] Cheng, Z., Sun, S., Du, X., Tang, Q., Shi, J., Liu, X., Jianrong, Q., "Microstructural evolution of a FeCo15Cr14Ni4Mo3 maraging steel with high ductility prepared by selective laser melting", Mater. Today Commun., 2022, 31, 103243. https://doi.org/10.1016/j.mtcomm.2022.103243

[21] de Melo, R. V., de Oliveira, C. A. S., Pofo, C. M., de Abreu, H. F. G., "Structural Study of Undeformed and Deformed Maraging C300 Steels Using X-ray Difraction Measurements", Metallogr. Microstruct. Anal., 2020, 9, 660–667. https://doi.org/10.21062/ujep/241.2019/a/1213-2489/MT/19/1/37

[22] Tillmann, W., Wojarski, L., Henning, T., "Investigation of joints from laser powder fusion processed and conventional material grades of 18MAR300 nickel maraging steel", Weld. World, 2021, 65, 1323-1331. https://doi.org/10.1007/s40194-021-01096-1

[23] Tian, Y., Palad, R., Aranas Jr, C., "Microstructural evolution and mechanical properties of a newly designed steel fabricated by laser powder bed fusion", Addit. Manuf., 2020, 36, 101495. https://doi.org/10.1016/j.addma.2020.101495

[24] Bai, Y., Yang, Y., Wang, D., Zhang, M., "Influence mechanism of parameters process and mechanical properties evolution mechanism of maraging steel 300 by selective laser melting", Mater. Sci. Eng. A, 2017, 703, 116-123. https://doi.org/10.1016/j.msea.2017.06.033

22

[25] Becker, T. H., DImitrov, Di., "The achievable mechanical properties of SLM produced maraging Steel 300 components", Rapid Prototyp. J., 2016, 22, 487-494. https://doi.org/10.1108/RPJ-08-2014-0096

[26] Casalino, G., Campanelli, S. L., Contuzzi, N., Ludovico, A. D., "Experimental investigation and statistical optimisation of the selective laser melting process of a maraging steel", Opt. Laser Technol., 2015, 65, 151-158. https://doi.org/10.1016/j.optlastec.2014.07.021

[27] de Souza, A. F., Al-Rubaie, K. S., Marques, S., Zluhan, B., Santos, E. C., "Effect of laser speed, layer thickness, and part position on the mechanical properties of maraging 300 parts manufactured by selective laser melting", Mater. Sci. Eng., A, 2019, 767, 138425. https://doi.org/10.1016/j.jmrt.2023.07.114

[28] Shamsdini, S. A. R., Shakerin, S., Hadadzadeh, A., Amirkhiz, B. S., Mohammadi, M., "A trade-off between powder layer thickness and mechanical properties in additively manufactured maraging steels", Mater. Sci. Eng. A, 2020, 776, 139041. https://doi.org/10.1016/j.msea.2020.139041

[29] Huang, W., Zhang, W., Chen, X., "Effect of SLM process parameters on relative density of maraging steel (18Ni-300) formed parts", IOP Conf. Ser.: Mater. Sci. Eng., 2020, 774, 1-8. https://doi.org/10.1088/1757-899X/774/1/012027

[30] Mugwagwa, L., Yadroitsev, I., Matope, S., "Effect of process parameters on residual stresses, distortions, and porosity in selective laser melting of maraging steel 300", Metals, 2019, 9, 1042. https://doi.org/10.3390/met9101042

[31] Suzuki, A., Nishida, R., Takata, N., Kobashi, M., Kato, M., "Design of laser parameters for selectively laser melted maraging steel based on deposited energy density", Addit. Manuf., 2019, 28, 160-168. https://doi.org/10.1016/j.addma.2019.04.018

[32] Mutua, J., Nakata, S., Onda, T., Chen, Z. C., "Optimization of selective laser melting parameters and influence of post heat treatment on microstructure and mechanical properties of maraging steel", Mater. Des., 2018, 139, 486-497. https://doi.org/10.1016/j.matdes.2017.11.042

[33] Hu, J., Zhang, L., Wang, X., Lin, W., Wei, P., Cao, Y., Zhang, J., Sun, K., "Effect of Heat Treatments on the Microstructure and Properties of 18Ni300 Maraging Steel Produced by Selective Laser Melting", Materials 2025, 18, 2284-2296. https://doi.org/10.3390/ma18102284

[34] Vishwakarma, J., Chattopadhyay, K., Santhi Srinivas, N. C., "Effect of build orientation on microstructure and tensile behaviour of selectively laser melted M300 maraging steel", Mater. Sci. Eng. A, 2020, 798, 140130. https://doi.org/10.1016/j.msea.2020.140130

[35] Yao, Y. , Wang, K., Wang, X., Li, L., Cai, W., Kelly, S., Esparragoza, N., Rosser, M., Yan, F., "Microstructural heterogeneity and mechanical anisotropy of 18Ni-330 maraging steel fabricated by selective laser melting: The effect of build orientation and height", J. Mater. Res., 2020, 35, 2065-2076. https://doi.org/10.1557/jmr.2020.126

[36] Patil, V.V.; Mohanty, C.P.; Prashanth, K.G. Parametric Optimization of Selective Laser Melted 13Ni400 Maraging Steel by Taguchi Method. J. Manuf. Mater. Process. 2024, 8, 52-70. https://doi.org/10.3390/jmmp8020052

[37] Tan, C., Zhou, K., Kuang, M., Ma, W., Kuang, T., "Microstructural characterization and properties of selective laser melted maraging steel with different build directions", Sci. Technol. Adv. Mater., 2018, 19, 746-758. https://doi.org/10.1080/14686996.2018.1527645

[38] Zetkova, I., Kučerová, L., Zetek, M., Monka, P., Daňa, M., "Study of 3D printing direction and effects of heat treatment on mechanical properties of MS1 maraging steel", Arch. Appl. Mech., 2019, 89, 791-804. https://doi.org/10.1007/s00419-018-1389-3

[39] Kannan, R., List, F., Joslin, C., Rossy, A. M., Nandwana, P., "Effect of volumetric energy density on microstructure and properties of grade 300 maraging steel fabricated by laser powder bed fusion", Metall. Mater. Trans. A, 2023, 54A, 1062-1069. https://doi.org/10.1007/s11661-023-06969-2

[40] Swain, S., Datta, S. & Roy, T. Microstructure and Mechanical Property Characterization of Additively Manufactured Maraging Steel 18Ni(300) Built Part. J. of Materi Eng and Perform, 2025, https://doi.org/10.1007/s11665-025-11239-w.

24

[41] Mechali, A., Hlinka, J., Hajnys, J.,Cegan, T.,Zelinka, J. Mesicek, J., Sajgalik, M., Petru, J., Research about SLM 3D printing-M300 maraging steel surface and post-processing characteristics, J. Adv. Manuf. Technol, 2025, 138, 709–724. https://doi.org/10.1007/s00170-025-15413-1

[42] Vahidshad, Y., Abrinia, C., Aalimehr P., (2024) Optimization of selective laser melting (SLM) process factors for 3D printing of maraging 300 steel parts via taguchi method, Journal of Space Science, Technology and Applications, 2024, 4, 52-63. https://doi.org/10.22034/jssta.2024.417595.1140

[43] Bai, Y., Wang, D., Yang, Y., Wang, H., "Effect of heat treatment on the microstructure and mechanical properties of maraging steel by selective laser melting", Mater. Sci. Eng. A, 2019, 760, 105-117. https://doi.org/10.1016/j.msea.2019.05.115

[44] Bai, Y., Zhao, C., Yang, J., Hong, R., Weng, C., Wang, H., "Microstructure and machinability of selective laser melted high-strength maraging steel with heat treatment", J. Mater. Process. Technol., 2021, 288, 116906. https://doi.org/10.1016/j.jmatprotec.2020.116906

[45] Vahidshad, Y., Fashi, A., "Characterization of the Mechanical Properties of Maraging 300 Alloy Produced by Selective Laser Melting Additive Manufacturing Method Used Digital Image Correlation Technique", Accepted Manuscript, Journal of Space Science, Technology and Applications, 2024, https://doi.org/10.22034/jssta.2024.450470.1157.

[46] Tekin, T., Ischia, G., Naclerio, F., Ipek, R., Molinari, A., "Effect of a direct aging heat treatment on the microstructure and the tensile properties of a 18Ni-300 maraging steel produced by laser powder bed fusion", Mater. Sci. Eng. A, 2023, 872, 144921. https://doi.org/10.1016/j.msea.2023.144921

[47] Mooney B., Kourousis, K. I., Raghavendra, R., "Plastic anisotropy of additively manufactured maraging steel: influence of the build orientation and heat treatments", Addit. Manuf., 2019, 25, 19-31. https://doi.org/10.1016/j.addma.2018.10.032

1